OPTOMECHANICS

Nano-acoustic resonator with ultralong phonon lifetime

Gregory S. MacCabe[1,2,3]*, Hengjiang Ren[1,2]*, Jie Luo[1,2]†, Justin D. Cohen[1,2]‡, Hengyun Zhou[1,2]§, Alp Sipahigil[1,2], Mohammad Mirhosseini[1,2], Oskar Painter[1,2,3]#

The energy damping time in a mechanical resonator is critical to many precision metrology applications, such as timekeeping and force measurements. We present measurements of the phonon lifetime of a microwave-frequency, nanoscale silicon acoustic cavity incorporating a phononic bandgap acoustic shield. Using pulsed laser light to excite a colocalized optical mode of the cavity, we measured the internal acoustic modes with single-phonon sensitivity down to millikelvin temperatures, yielding a phonon lifetime of up to $\tau_{\mathrm{ph},0} \approx 1.5$ seconds (quality factor $Q = 5 \times 10^{10}$) and a coherence time of $\tau_{\mathrm{coh},0} \approx 130$ microseconds for bandgap-shielded cavities. These acoustically engineered nanoscale structures provide a window into the material origins of quantum noise and have potential applications ranging from tests of various collapse models of quantum mechanics to miniature quantum memory elements in hybrid superconducting quantum circuits.

In optics, geometric structuring at the nanoscale has become a powerful method for modifying the electromagnetic properties of a bulk material, leading to metamaterials capable of manipulating light in unprecedented ways (1). In the most extreme case, photonic bandgaps can emerge in which light is forbidden from propagating, markedly altering the emission of light from within such materials (2). More recently, a similar phononics revolution (3) in the engineering of acoustic waves has led to a variety of new devices, from thermal crystals for controlling the flow of heat (3) to phononic topological insulators for scattering-free transport of acoustic waves (4).

Phononic bandgap structures, similar to their electromagnetic counterparts, can be used to modify the emission or scattering of phonons. These ideas have recently been explored in quantum optomechanics (5–8) and electromechanics (9) experiments to greatly reduce the mechanical coupling to the thermal environment through acoustic radiation. To date, far less attention has been paid to the impact of geometry and phononic bandgaps on acoustic material absorption and related noise effects (10, 11). Fundamental limits to sound absorption in solids are known to result from the anharmonicity of the host crystal lattice (12, 13). At low temperatures T, in the Landau-Rumer regime ($\omega \tau_{\mathrm{th}} \gg 1$), where the thermal phonon relaxation rate (τ_{th}^{-1}) is much smaller than the acoustic frequency (ω), a quantum model of three-phonon scattering can be used to describe phonon-phonon mixing that results in damping and thermalization of acoustic modes (12, 13). Landau-Rumer damping scales approximately as T^{α}, where $\alpha \approx 4$ depends upon the phonon dispersion and density of states (DOS) (13). At the very lowest lattice temperatures ($\lesssim 10$ K), where Landau-Rumer damping has dropped off, a residual damping emerges due to material defects. These two-level system (TLS) defects (14), typically found in amorphous materials, correspond to a pair of nearly degenerate local arrangements of atoms in the solid, which can have both an electric and an acoustic transition dipole, and couple to both electric and strain fields. Recent theoretical analysis shows that TLS interactions with acoustic waves can be substantially altered in a structured material (10).

Here we explore the limits of acoustic damping and coherence of a microwave-frequency acoustic nanocavity with a phononic crystal shield that possesses a wide bandgap for all polarizations of acoustic waves. Our nanocavity, formed from an optomechanical crystal (OMC) nanobeam resonator (5), supports an acoustic breathing mode at $\omega_{\mathrm{m}}/2\pi \approx 5$ GHz and a colocalized optical resonant mode at $\omega_{\mathrm{c}}/2\pi \approx 195$ THz ($\lambda_{\mathrm{c}} \approx 1550$ nm), which allows us to excite and read out mechanical motion using radiation pressure from a pulsed laser source. This minimally invasive pulsed measurement technique avoids a slew of parasitic damping effects—typically associated with electrode materials and mechanical contact (15), or probe fields for continuous readout—and allows for the sensitive measurement of motion at the single-phonon level (16). The results of acoustic ringdown measurements at millikelvin temperatures show that damping due to radiation is effectively suppressed by the phononic shield, with breathing-mode quality factors reaching $Q = 4.9 \times 10^{10}$, corresponding to a frequency-Q product of $f - Q = 2.6 \times 10^{20}$.

The devices studied in this work are fabricated from the 220-nm device layer of a silicon-on-insulator (SOI) microchip. [See (17) for materials and methods.] In Fig. 1, A and B, we show scanning electron microscope (SEM) images of a single fabricated device, which consists of a coupling optical waveguide, a pair of nanobeam OMC cavities that support both a microwave acoustic and an optical resonant mode, and the acoustic shield that connects the cavities to the surrounding chip substrate. Figure 1C shows finite-element method (FEM) simulations of the microwave acoustic breathing mode and fundamental optical mode of the nanobeam cavity. The design of the OMC cavities, detailed in (5), provide strong localization and overlap of the breathing mode and the fundamental optical mode, resulting in a vacuum optomechanical coupling rate (5) between photons and phonons of $g_0/2\pi \approx 1$ MHz.

To minimize mechanical clamping losses, the nanobeam is anchored to the Si bulk with a periodic cross structure (5). FEM numerical modeling indicates that the cross shield must be carefully designed to provide protection against nanometer-scale disorder, which is inherently introduced during device fabrication (see materials and methods, section II). As shown in Fig. 1, D to F, by including the finite radius of curvature (35 nm) of the corners of the cross shape present in fabricated structures, we could increase the acoustic bandgap to a 3-GHz bandwidth and accurately align the breathing acoustic mode of the nanobeam to the center of the shield gap. Reevaluation of devices measured in (16), which did not factor in the finite radius curvature of the fabricated cross shield, indicate a misalignment of the acoustic bandgap with the nanobeam mode.

To investigate the efficacy of the newly designed acoustic shielding in practice, we fabricated and characterized arrays of devices with a scaling of the cross period number from $N_{\mathrm{shield}} = 0$ to 10, with all other design parameters held constant. Optical measurements of the acoustic properties of the OMC cavities are performed at millikelvin temperatures in a dilution refrigerator, with a lensed optical fiber used to couple light into and out of each device (16). In a first set of measurements of acoustic energy damping, we use a single pulsed laser scheme to perform both excitation and readout of the breathing mode. In this scenario, depicted in Fig. 2, A and B, the laser frequency (ω_{l}) is tuned to the red motional sideband of the OMC cavity optical resonance, $\Delta \equiv \omega_{\mathrm{c}} - \omega_{\mathrm{l}} \approx + \omega_{\mathrm{m}}$, and is pulsed on for a duration T_{pulse} and then off for a variable time τ. This produces a periodic train of photon pulses
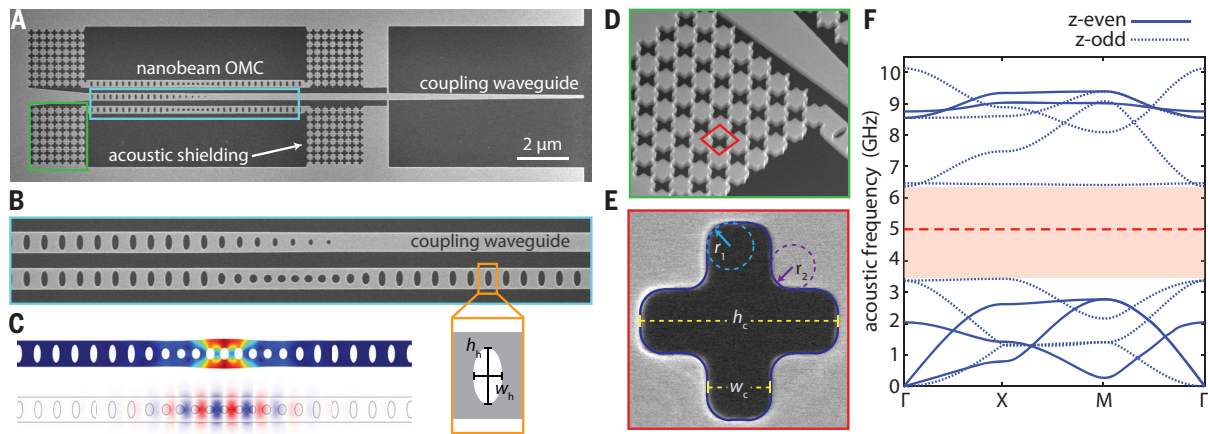
Fig. 1. Nanobeam optomechanical crystal and phononic shield design.
(**A**) Scanning electron microscope (SEM) image of a full nanobeam optomechanical crystal (OMC) device fabricated on SOI with $N = 7$ periods of acoustic shielding. A central coupling waveguide allows for fiber-to-chip optical coupling as well as side-coupling to individual nanobeam OMC cavities. (**B**) SEM image of an individual nanobeam OMC and the coupling waveguide, with enlarged illustration of an individual unit cell in the end-mirror portion of the nanobeam. (**C**) FEM simulations of the mechanical (top; total displacement) and optical (bottom; transverse electric field) modes of interest in the nanobeam. Distortion of the mechanical displacement profile is exaggerated for clarity. (**D**) SEM image showing the nanobeam clamping geometry. (**E**) SEM image of an individual unit cell of the cross-crystal acoustic shield. The dashed lines show fitted geometric parameters used in simulation, including cross height ($h_c = 474$ nm), cross width ($w_c = 164$ nm), inner fillet radius (r_1), and outer fillet radius (r_2). (**F**) Simulated acoustic band structure of the realized cross-crystal shield unit cell, with the full acoustic bandgap highlighted in pink. Solid (dotted) lines correspond to modes of even (odd) symmetry in the direction normal to the plane of the unit cell. The dashed red line indicates the mechanical breathing-mode frequency at $\omega_m/2\pi = 5.0$ GHz.
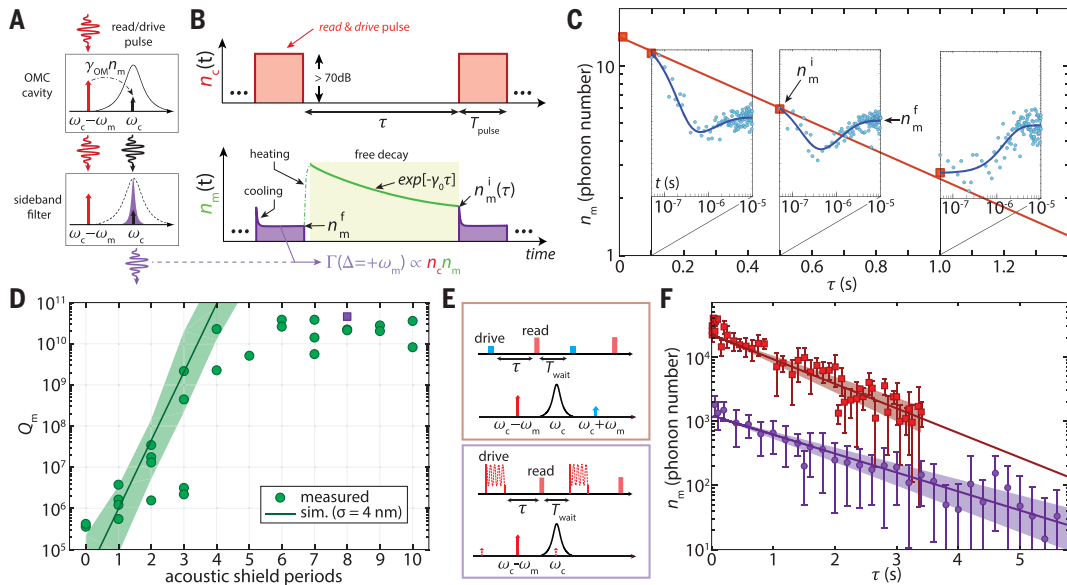

Fig. 2. Ringdown measurements of the acoustic breathing mode.
(**A**) Illustration showing the red-detuned ($\Delta = +\omega_m$) optical drive and sideband optical filtering used to realize effective phonon counting measurement. (**B**) Illustration of the ringdown measurement performed using a single pulsed laser for both excitation and readout. Top (bottom): Intracavity photons (phonons) versus time. (**C**) Ringdown measurements of a seven-shield device (device C) for readout pulse amplitude of $n_c = 320$. The series of inset panels show the measured (and fit; solid blue curve) anti-Stokes signal during the optical pulse at a series of pulse delays. (**D**) Plot of the measured breathing mode Q-factor versus number of acoustic shield periods N_{shield}. The solid green line is a fit to the corresponding simulated radiation-limited Q-factor for devices with standard deviation (SD) $\sigma = 4$ nm disorder in hole position and size, similar to the value measured from device SEM image analysis. The shaded green region corresponds to the range of simulated Q values (ensemble size 10) within 1 SD of the mean. The square purple data point represents the measured Q in (F). (**E**) Acoustic excitation is performed coherently by using either a blue-detuned pump (upper diagram) to drive the breathing mode into self-oscillation, or using a radiofrequency-modulated red-detuned pump (18) (lower diagram). See materials and methods, section V, for details of the coherent excitation and readout parameters. (**F**) Ringdown measurements performed on an eight-shield device (device D) at large phonon amplitude. For blue-detuned driving (red squares), the fit decay rate is $\gamma_0/2\pi = (0.122 \pm 0.020)$ Hz. For modulated-pump driving (purple circles), the fit decay rate is $\gamma_0/2\pi = (0.108 \pm 0.006)$ Hz. The error bars are 90% confidence intervals of the measured values of n_m^i. The shaded regions are the 90% confidence intervals for the exponential fit curves.
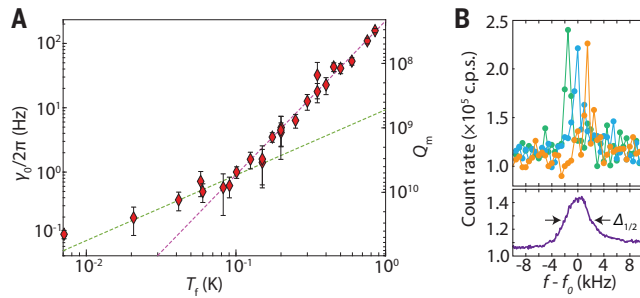
Fig. 3. Temperature dependence of acoustic damping and frequency jitter. (**A**) Plot of the measured breathing-mode energy damping rate, $\gamma_0/2\pi$, as a function of fridge temperature (T_f). Dashed green (magenta) curve is a fit with temperature dependence $\gamma_0 \sim T_f^{1.01}$ ($\gamma_0 \sim T_f^{2.39}$). Error bars are 90% confidence intervals of the exponential fit to measured ringdown curves. (**B**) Two-tone coherent spectroscopy signal. Upper plot: Three individual spectra of rapid frequency sweeps with a frequency step size of 500 Hz and dwell time of 1 ms (resolution bandwidth RBW ≈0.5 kHz). Lower plot: Average spectrum of rapid-scan spectra taken over minutes, showing broadened acoustic response with FWHM linewidth of $\Delta_{1/2}/2\pi = 4.05$ kHz. The large on-resonance response corresponds to an estimated optomechanical cooperativity of $C \equiv \gamma_{OM}/(\gamma_0 + \gamma_p) \gtrsim 1.1$, consistent with the predicted magnitude of back-action damping $\gamma_{OM}/2\pi \approx 817$ Hz and bath-induced damping $\gamma_p/2\pi \approx 120$ Hz at the measurement pump power level $n_c = 0.1$. Data presented in (A) and (B) are for device D.

due to anti-Stokes scattering of the probe laser that are on-resonance with the optical cavity. The anti-Stokes scattered photons are filtered from the probe laser and sent to a single photon detector, producing a photon count rate proportional to the number of phonons in the acoustic resonator (see materials and methods, section III). The resulting intracavity phonon pulse shape, illustrated in Fig. 2B, has a shape determined by a competition between optical absorption–induced heating and optomechanical back-action cooling (16). The net result is that the acoustic mode is excited to a small thermal population at the end of the readout pulse, with free decay of the phonon number amplitude in between pulses (see materials and methods, section IV). Plotting the initial mode occupancy at the beginning of the readout pulse (n_m^i) versus delay time τ between pulses results in a ringdown curve of the stored phonon number in the breathing mode, an example of which is displayed in Fig. 2C for a device with $N_{shield} = 7$.

Performing a series of ringdown measurements over a range of devices with varying N_{shield}, and fitting an exponential decay curve to each ringdown, we produce the Q-factor plot in Fig. 2D. We observe an initial trend in Q-factor versus shield number that rises on average exponentially with each additional shield period (×5.5 per period, in good correspondence with the FEM modeling) and then saturates for $N_{shield} \geq 5$ to $Q_m \gtrsim 10^{10}$. As indicated in Fig. 2C, these Q values correspond to ringdown of small, near-single-phonon–level amplitudes. We also perform ringdown measurements at high phonon amplitude using two additional methods displayed schematically in Fig. 2E (see materials and methods, section V). These methods use two laser tones to selectively excite the acoustic breathing

mode using a ×1000 weaker excitation and readout optical pulse amplitude ($n_c \lesssim 0.3$). The measured ringdown curves, displayed in Fig. 2F, show the decay from initial phonon occupancies of 10^3 to 10^4 of an eight-shield device (device D; square purple data point in Fig. 2D). The two methods yield similar breathing-mode energy decay rates of $\gamma_0/2\pi = 0.108$ Hz and 0.122 Hz, the smaller of which corresponds to a Q-value of $Q_m = 4.92^{+0.39}_{-0.26} \times 10^{10}$ and a phonon lifetime of $\tau_{ph,0} = 1.47^{+0.09}_{-0.08}$ s. Comparing all three excitation methods with widely varying optical absorption–heating and phonon amplitude, we consistently measure $Q_m \gtrsim 10^{10}$ for devices with $N_{shield} \geq 5$. This represents an improvement by more than three orders of magnitude compared to previous measurements of devices with nonoptimized acoustic shielding (16).

To understand the origin of the residual damping for large N_{shield} we also measured the temperature dependence of the energy damping rate for a number of the high-Q, large N_{shield} devices. In Fig. 3A, we plot the energy damping rate versus fridge temperature (T_f) for the highest-Q eight-shield device (device D), typical of all of these types of devices that we measured, which shows an approximately linear rise in temperature up to $T_f \approx 100$ mK and then a much faster $\sim (T_f)^{2.4}$ rise in the damping above this temperature. This rather anomalous temperature scaling of the damping does not fit the standard damping models relating to three-phonon scattering, and estimates of the magnitude of Landau-Rumer damping of the breathing mode indicate that three-phonon scattering in Si is far too weak at $T_f \lesssim 1$ K to explain the absolute level of measured damping (see materials and methods, section VI). Canonical models of TLS-induced damping also fail to predict the

measured temperature scaling of the damping. Analysis of the interactions of TLS in the surface of the silicon with the localized acoustic modes in the confined geometry of the OMC cavity sructure, however, show that TLS interactions can explain all of the observed breathing-mode behavior when taking into account the highly modified density of phonon states in the shielded OMC cavity (see supplementary text, sections VII and VIII). In particular, we find that damping due to nearly resonant TLS is suppressed owing to the bandgap of the phononic shield and that relaxation damping from nonresonant TLS can explain the magnitude and low-temperature dependence of the breathing-mode damping and the lack of saturation of the damping with both temperature and acoustic amplitude.

In addition to energy damping, the coherence of the high-Q breathing modes is also of interest. Using the same pump-probe excitation method (18) as in the ringdown measurements of Fig. 2, E and F, we can measure the breathing-mode acoustic spectrum by sweeping the probe tone across the acoustic resonance. Figure 3B shows the measured acoustic spectrum of device D at the fridge base temperature $T_f = 7$ mK and a low pump power of $n_c = 0.1$. The top plot shows a series of rapid spectral scans (40 ms per scan), which captures a jittering narrow acoustic line. Scanning more slowly than the 40-ms per scan begins to introduce broadening into the single-scan spectral line, providing a rough estimate for the (inverse) bandwidth of the frequency jitter noise of the breathing mode. An ensemble average of these scans, taken over several minutes, yields a broadened acoustic full width at half-maximum (FWHM) linewidth of $\Delta_{1/2}/2\pi = 4.05$ kHz (bottom plot of Fig. 3B). This behavior is characteristic of coherent-like frequency noise, such as flicker or low-frequency telegraph noise. In this case, the coherence time is given by $\tau_{coh,0} \approx 4(\ln(2))^{1/2}/\Delta_{1/2} \approx 130$ μs (19, 20). The likely source of this noise is again fluctuating TLS (see supplementary text, section VIII).

Several subtle points regarding the energy decay and coherence measurements should be noted. First, the breathing-mode spectral linewidth (and thus coherence time) is measured in the presence of a weak laser pump field, in contrast to energy decay measurements, in which the laser is pulsed off. Although we did not observe a power dependence of the measured time-average acoustic linewidth, the influence of the laser field on the acoustic mode coherence time cannot be ruled out. Second, the pump-probe technique used to measure the acoustic spectrum excites the breathing mode to an estimated mode occupancy of order 1000; of relevance to many quantum applications is the single-phonon coherence time.

With the recent demonstration of strong dispersive coupling of a superconducting qubit to similar nanomechanical acoustic cavities (21), measurement of single-phonon coherence time in the absence of light fields should be possible. Additionally, the low-frequency character of the frequency noise measured in this work indicates that the acoustic coherence time may be substantially increased toward the energy decay time through techniques such as dynamic decoupling (22). Finally, the attribution of the residual damping and the frequency jitter noise to surface TLS indicates that further study of the silicon surface composition may lead to a better understanding of the microscopic nature of the TLS and help identify further surface preparation methods for their removal (see materials and methods, section I, and supplementary text, section VIII).

More generally, the results presented here show that the advanced methods of nanofabrication and cavity optomechanics provide a new toolkit to explore quantum acoustodynamics in solid-state materials (23). For example, continued studies of phononic engineered structures in the quantum regime may lead to techniques for modifying the behavior of quasiparticles in superconductors (24), new approaches for mitigating decoherence (noise) in superconducting (25) and color center (26) qubits, and even new TLS–acoustic cavity qubit architectures (27). The extremely small motional mass [$m_{eff} = 136$ fg (5)] and narrow linewidth of the OMC cavity also make it ideal for precision mass sensing (28) and in exploring limits to alternative quantum collapse models (29). Perhaps most intriguing is the possibility of creating a hybrid quantum architecture consisting of acoustic and superconducting quantum circuits (21, 30), where the small scale, reduced cross-talk, and ultralong coherence time of quantum acoustic devices may provide substantial improvements in connectivity and performance of current quantum hardware.

REFERENCES AND NOTES

1. J. D. Joannopoulos, S. G. Johnson, J. N. Winn, R. D. Meade, *Photonic Crystals: Molding the Flow of Light* (Princeton Univ. Press, ed. 2nd, 2008).
2. S. John, J. Wang, *Phys. Rev. B Condens. Matter* **43**, 12772–12789 (1991).
3. M. Maldovan, *Nature* **503**, 209–217 (2013).
4. J. Cha, K. W. Kim, C. Daraio, *Nature* **564**, 229–233 (2018).
5. J. Chan, A. H. Safavi-Naeini, J. T. Hill, S. Meenehan, O. Painter, *Appl. Phys. Lett.* **101**, 081115 (2012).
6. P.-L. Yu et al., *Appl. Phys. Lett.* **104**, 023510 (2014).
7. Y. Tsaturyan, A. Barg, E. S. Polzik, A. Schliesser, *Nat. Nanotechnol.* **12**, 776–783 (2017).
8. A. H. Ghadimi et al., *Science* **360**, 764–768 (2018).
9. M. Kalaee et al., *Nat. Nanotechnol.* **14**, 334–339 (2019).
10. R. O. Behunin, F. Intravaia, P. T. Rakich, *Phys. Rev. B* **93**, 224110 (2016).
11. B. D. Hauer, P. H. Kim, C. Doolin, F. Souris, J. P. Davis, *Phys. Rev. B* **98**, 214303 (2018).
12. L. Landau, G. Rumer, *Phys. Z. Sowjet.* **11**, 18 (1937).
13. G. P. Srivastava, *The Physics of Phonons* (Taylor & Francis, 1990).
14. W. A. Phillips, *Rep. Prog. Phys.* **50**, 1657–1708 (1987).
15. S. Galliou et al., *Sci. Rep.* **3**, 2132 (2013).
16. S. M. Meenehan et al., *Phys. Rev. X* **5**, 041002 (2015).
17. See supplementary materials.
18. A. H. Safavi-Naeini et al., *Nature* **472**, 69–73 (2011).
19. G. Di Domenico, S. Schilt, P. Thomann, *Appl. Opt.* **49**, 4801–4807 (2010).
20. P. J. J. O'Malley, thesis, University of California, Santa Barbara (2016).
21. P. Arrangoiz-Arriola et al., *Phys. Rev. X* **8**, 031007 (2018).
22. J. Bylander et al., *Nat. Phys.* **7**, 565–570 (2011).
23. W. H. Renninger, P. Kharel, R. O. Behunin, P. T. Rakich, *Nat. Phys.* **14**, 601–607 (2018).
24. K. Rostem, P. J. de Visser, E. J. Wollack, *Phys. Rev. B* **98**, 014522 (2018).
25. J. M. Martinis, A. Megrant, UCSB final report for the CSQ program: Review of decoherence and materials physics for superconducting qubits. arXiv:1410.5793 (2014).
26. Y.-I. Sohn et al., *Nat. Commun.* **9**, 2012 (2018).
27. T. Ramos, V. Sudhir, K. Stannigel, P. Zoller, T. J. Kippenberg, *Phys. Rev. Lett.* **110**, 193602 (2013).
28. M. S. Hanay et al., *Nat. Nanotechnol.* **10**, 339–344 (2015).
29. S. Nimmrichter, K. Hornberger, K. Hammerer, *Phys. Rev. Lett.* **113**, 020405 (2014).
30. M. H. Devoret, R. J. Schoelkopf, *Science* **339**, 1169–1174 (2013).
31. G. S. MacCabe, H. Ren, J. Luo, J. D. Cohen, H. Zhou, A. Sipahigil, M. Mirhosseini, O. Painter, Data for "Nano-acoustic resonator with ultralong phonon lifetime," Version 1, Zenodo (2020); http://doi.org/.